Song *et al. Chin. J. Mech. Eng.* (2020) 33:17
https://doi.org/10.1186/s10033-020-0436-5

Chinese Journal of Mechanical Engineering

ORIGINAL ARTICLE Open Access

Dynamic Analysis and Performance Verification of a Novel Hip Prosthetic Mechanism

Majun Song, Sheng Guo*, Xiangyang Wang and Haibo Qu

Abstract

To assist an amputee in regaining his or her daily quality of life, based on analysis of the motion characteristics of the human hip, a 2-UPR/URR parallel mechanism with a passive limb was designed. The inverse kinematics of this mechanism was analyzed based on a closed-loop vector method. The constrained Jacobian matrix and kinematic Jacobian matrix of each limb were then analyzed, and a 6×6 fully Jacobian matrix was constructed. Based on this, kinematic performances were analyzed and summarized. Finally, the dynamic model of the mechanism was constructed based on the virtual work principle, and its theoretical solution was compared with the numerical results, which were obtained in a simulation environment. Results showed that the prosthetic mechanism had a larger rotating workspace and better mechanical performance, which accorded a range of motion and bearing capacity similar to that of the human hip in multiple gait modes. Moreover, the validity of the dynamic model and inverse kinematics were verified by comparing the theoretical and simulation results. Furthermore, with flexion and extension, the torque change in the hip prosthetic mechanism was similar to that of the human hip, which demonstrated the feasibility of the hip prosthetic mechanism and its good dynamic performance.

Keywords: Screw theory, Prosthetic hips, Workspace, Buckling analysis, Virtual work principle, Dynamics

1 Introduction

The main purpose of prosthetic mechanisms is to restore the functional motion of amputees in daily life, which can effectively compensate for the lost limbs of the amputee. With the rise in living standards, traditional prostheses that serve only as auxiliary support can no longer meet the requirements for movement of amputees. With the widespread application of robots in recent years, robotic prostheses [1, 2] have been extensively studied, especially for prosthetic mechanisms. Nelson et al. [3] designed a prosthesis, named Helix 3D, for amputees with hip dissociation, which is a serial mechanism that can only realize a single degree-of-freedom (DOF). Maja et al. [4] synthesized a hip prosthesis and conducted its periodic gait experiment by using wireless sensors. Hanz et al. [5] designed a hip prosthetic mechanism that has two DOFs in the sagittal plane. The control strategy was built and implemented to test its motion performance. However, the stiffness of these prosthetic mechanisms was comparatively low owing to the open-loop structure, and the limited DOF could not meet the movement requirements of the human hip. In order to achieve the motion characteristics of the human hip and improve its stiffness, Gu [6] designed a multi-DOF humanoid robot with a serial structure similar to the lower limbs of the human body, although it is rather complicated and heavy due to its excessive components. Hence, it is essential to design a hip prosthesis with multi-DOFs, good kinematics, and dynamic performance.

To achieve multi-DOFs and increase structural stiffness, parallel mechanisms have been applied in the design of the hip prosthesis. Its performance analyses have also been carried out by the designers. Cheng et al. [7] designed a 3-SPS/PS hip parallel mechanism with its

*Correspondence: shguo@bjtu.edu.cn
School of Mechanical, Electronic and Control Engineering, Beijing Jiaotong University, Beijing 100044, China

singularity analyzed using Grassmann line geometry. Due to the existence of the spherical joints, its stability would become poor when loaded. Sellaouti et al. [8] designed a bipedal walking robot with a 3-DOF parallel mechanism, which was a planar mechanism. The stability of the robot worsens during walking. Wang et al. [9] designed a 3R1T bionic parallel mechanism at the hip, and the kinematics and statics were analyzed. However, the presence of more actuators made it unfavorable for analysis of the dynamics and implementation of a control strategy for the mechanism.

In this paper, motion characteristics of the human hip were tested and analyzed via motion capture device, and a novel 2-DOF purely rotational parallel mechanism with a passive limb was synthesized by applying screw theory. The proposed mechanism acted as a hip prosthesis to fulfill the movement function of the human hip. The introduced passive limb not only enhanced the stiffness and stability of the prosthetic mechanism, but also reduced the control difficulty due to the employment of fewer motors. This paper is organized as follows: Configuration syntheses of active and passive limbs are illustrated in Section 2 based on the proposed design principles. From among the results, a parallel mechanism was selected as our hip prosthesis. In Section 3, inverse kinematics of the proposed mechanism are derived. The method of building the fully Jacobian matrix is presented in Section 4. In Section 5, its workspace, stiffness, bearing capacity, and dexterity are analyzed. The dynamic modeling process is shown in Section 6. The numerical and theoretical results are compared in Section 7. Finally, conclusions are drawn in Section 8.

2 2-UPR/URR Hip Parallel Mechanism

2.1 Design Demand Analysis Based on Kinematics of the Human Body

Based on the human musculoskeletal anatomy and human rehabilitation kinematics [10], the motion characteristics of the human hip, which has three spatial rotational DOFs around the horizontal, sagittal, and vertical axes, were analyzed as shown in Figure 1.

However, the main locomotor expression [11] of a hip in daily life is characterized by flexion, extension, abduction, and adduction, as shown in Figure 2(a) and 2(b); intorsion and extorsion can be neglected. Therefore, a hip prosthetic mechanism is designed to assist the amputee to restore the lost motion functions of flexion, extension, abduction, and adduction of the hip.

MotionAnalysis was used to test the gait data of inverse kinematics of the subjects, whose height and mass were 1.76 m and 80 kg, respectively, as shown in Figure 3. The ultimate rotational angles of the hip in multiple gait modes were tested, as shown in Table 1.

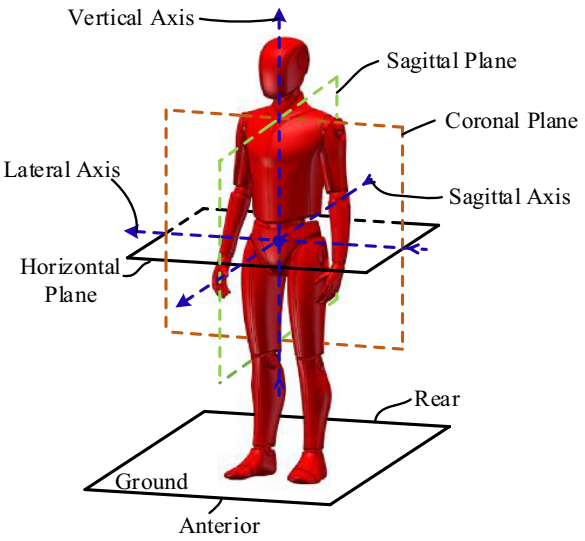

Figure 1 Human anatomical planes

Parallel mechanisms have advantages such as multiple DOFs and high bearing capacity. The designed hip prosthetic parallel mechanism should have a rotational ability around the lateral and sagittal axes, where the minimum range of rotational angles should be, respectively, $-22°$ to approximately $33°$ and $-7°$ to approximately $6°$. Meanwhile, it should also have sufficient stiffness and bearing capacity, which can give it good stability when supporting the human body. Although the maximum angles of intorsion and extorsion of the hip can be up to $45°$, this is only in a special state. However, the motion performances of the intorsion and extorsion are not active during the normal gait, as mentioned above; thus, the motion performances of intorsion and extorsion were not considered in the design of the hip prosthetic mechanism in this paper.

2.2 Configuration Synthesis

As shown in Section 2.1, to design a hip prosthetic parallel mechanism, five design guidelines should be followed:

1) In order to simplify the mechanism and ensure its effective motion characteristics, the designed hip prosthetic parallel mechanism consists of a passive limb and two actuating limbs.
2) Since the thigh is similar to a fixed-length binary rod, the function of the passive limb is to restrict its movement along the limb, i.e., there is no prismatic pair in the passive limb. In addition, the length of the passive limb is equal to the size of the human thigh. Moreover, spherical and universal joints cannot be the middle pair of each limb.

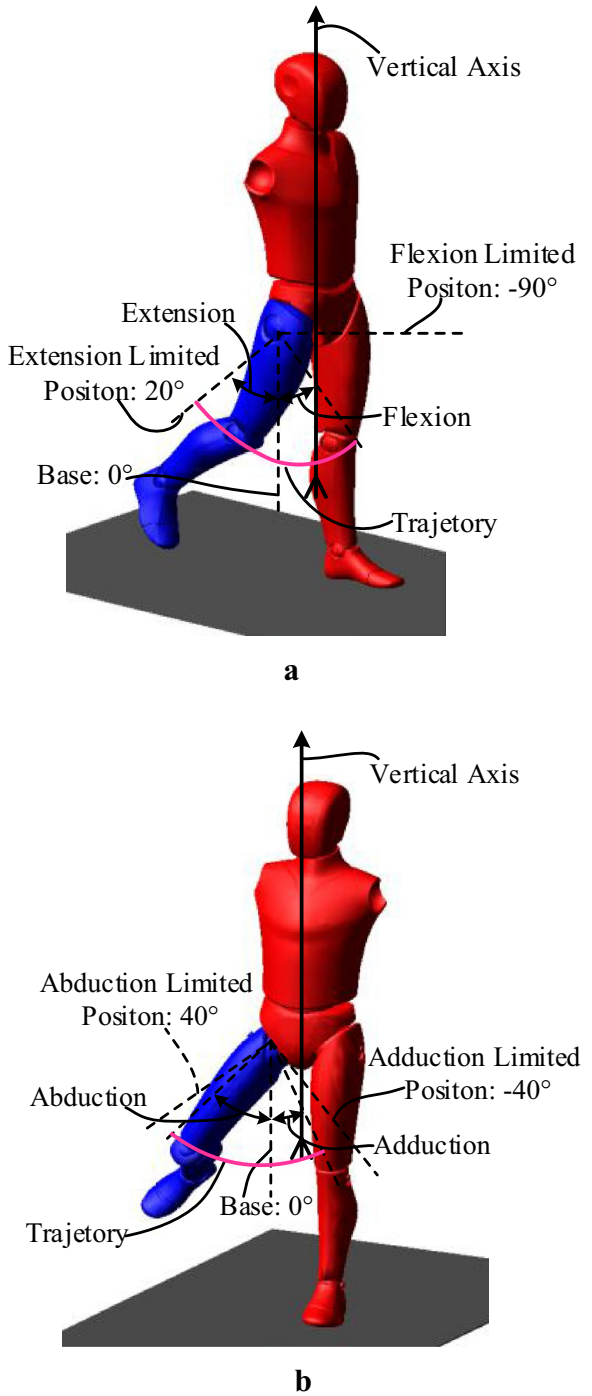

Figure 2 Motion characteristics of a human hip joint: **a** flexion and extension; **b** abduction and adduction

3) Configurations of the actuating limbs are the same, and they are distributed symmetrically to the plane where the passive limb is located.

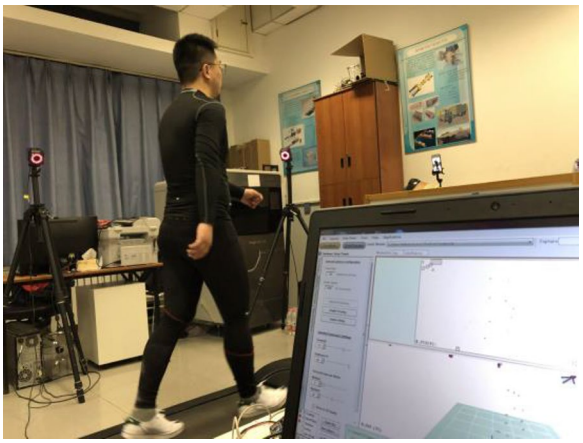

Figure 3 Testing platform for human gait

Table 1 Ultimate angles of the hip in multi-modes gait

Motion	No-loading		20 kg-loading	
	1.5 m/s	3.0 m/s	1.5 m/s	3.0 m/s
Flexion	22.5°	31.0°	24.5°	33.0°
Extension	− 21.5°	− 8.0°	− 14.0°	− 4.0°
Adduction	6.0°	6.0°	6.0°	6.0°
Abduction	− 7.0°	− 7.0°	− 5.5°	− 5.5°
Intorsion	2.3°	2.0°	2.2°	1.9°
Extorsion	− 3.4°	− 3.0°	− 3.0°	− 3.0°

4) To better mimic the contraction and extension of related muscles, the middle kinematic pair in each actuating limb sets as the prismatic pair.
5) To achieve the rotational angles of the hip, two revolute pairs that parallel to lateral and sagittal axes should be connected with the fixed base.

Based on this, the connectivity of the mechanism can be solved by the modified enumeration methodology:

$$\sum_{k=1}^{N} C_k = F_D + dL + \eta, \tag{1}$$

where C_k is the connectivity of the kth limb, F_D is the DOFs of the mechanism, d is the mechanism order, L is the number of closed-loop mechanisms, and η is the number of redundant DOFs of the mechanism. Then, in terms of Eq. (1), the classifications of connectivity of each limb are: $(C_1, C_2, C_3) = (6, 3, 3) = (4, 4, 4) = (2, 5, 5)$.

It was assumed that the available types of joints were R (Revolute), P (Prismatic), U (Universal), C (Cylinder), and S (Spherical). Based on connectivity, the synthesis of the actuating and passive limbs are shown in Tables 2, 3.

Table 2 Configuration synthesis of the passive limb

Motion characteristics	Joints	Configurations of passive limb
2R	1	$(RR)_{\perp}U$
3R	1,2	S, $(RR)_{\perp}R$, UR, $(RR)_{\perp}U$, SR, UU, $(RR)\perp S$, SU
	3	$UR_{\perp}R$, $((RR)_{\perp}R)_{\perp}U$, URU, UUR, US, SRR
	4,5,6	$(URR)_{\perp}R$, $((RR)_{\perp}R)_{\perp}R$, $(RR)\perp RRR$

In Tables 2 and 3, $(\cdot)_{\perp}$ indicates that the axes of two kinematic pairs in parentheses were orthogonal, and they were installed together on the fixed base and served as a joint. $\perp$ Denotes that the axis of kinematic pair was orthogonal with the plane on which the fixed base was located. * Denotes the axis of kinematic pairs in parentheses along the limb.

According to the configurations of the limbs, a parallel mechanism was designed that met the motion characteristics of the human hip following these two steps:

1) The terminals of the passive or actuating limb had least two spatial rotational DOFs.
2) A parallel mechanism with two spatial rotational DOFs was synthesized based on the mathematical intersection operation [12].

Generally, for good stability and better motion characteristics, each limb of the parallel mechanism was consistently arranged with three joints. By analysis and comparison for the configuration of limbs under design guidelines, the configuration of $UR_{\perp}R$ was selected as the passive limb, and the configuration of UPR was selected as the actuating limb. Therefore, the hip parallel prosthetic mechanism designed in this paper was called a 2-UPR/URR parallel mechanism, as shown in Figure 4, which had the motions of flexion, extension, abduction, and adduction.

The schematic diagram is shown in Figure 5. The prosthesis can rotate around both the X-axis and the Y-axis.

Our prosthetic consisted of a fixed base, a moving platform, a passive limb, and two actuating limbs, and the driving limbs were arranged symmetrically along the X-Z plane. The universal and revolute pairs were connected to the fixed base and the moving platform, respectively, in each limb, and the axis of revolute was parallel to the outboard axis of the universal one. The upper and lower rods in the passive limb were connected by a revolute, and the axis was collinear with the direction of the passive limb. The cylinder and piston in the actuating limb were connected by a prismatic, whose moving direction was along the direction of the actuating limb, and it also served as an actuator.

In Figure 5, the fixed base $\Delta A_1A_2A_3$ and the moving platform $\Delta B_1B_2B_3$ are equilateral triangles and their side lengths are $2a$ and $2b$, respectively; the origin O of the fixed frame O-XYZ is located at the center of A_2A_3, the direction of X and Y axis is along OA_1 and OA_2, and the direction of Z is obtained by the right-hand rule. The origin o of the moving frame o-xyz is located at the center of B_2B_3, the direction of x- and y-axes are along oB_1 and oB_2, respectively, and the direction of z is obtained by the right-hand rule.

3 Inverse Kinematic Analysis

For the parallel mechanism, the final location was obtained by a rotation of α about the x-axis, followed by a second rotation of β about the displaced y'-axis. The resulting rotation matrix was derived based on a Euler angle representation [13], as follows,

$$\boldsymbol{R}_B^A = \begin{bmatrix} \cos\beta & 0 & \sin\beta \\ \sin\alpha\sin\beta & \cos\alpha & -\cos\beta\sin\alpha \\ -\cos\alpha\sin\beta & \sin\alpha & \cos\alpha\cos\beta \end{bmatrix}, \tag{2}$$

assuming that the position vector of point o expressed in the fixed frame is $\boldsymbol{p}=[x_p, y_p, z_p]$. The position vector of point A_i is $\boldsymbol{a}_1$, $\boldsymbol{a}_2$, and $\boldsymbol{a}_3$, which can be obtained easily in Figure 5. B_i with respect to the fixed frame is given by:

$$\begin{bmatrix} \boldsymbol{b}_1 \\ \boldsymbol{b}_2 \\ \boldsymbol{b}_3 \end{bmatrix} = \begin{bmatrix} x_p + bc\beta & y_p + bs\alpha s\beta & z_p - bc\alpha s\beta \\ x_p & y_p + bc\alpha & z_p + bs\alpha \\ x_p & y_p - bc\alpha & z_p - bs\alpha \end{bmatrix}. \tag{3}$$

A vector-loop equation of a Limb i can then be written as:

Table 3 Configuration synthesis of the actuating limb

Motion characteristics	Joints	Configuration of actuating limbs
2R1T	2	$(RR)_{\perp}P$, UP
3R1T	2	SP, $(RR)_{\perp}C$, UC, SC
	3	$(RR)_{\perp}R_{\perp}P$, $(RR)_{\perp}PR$, $UR_{\perp}P$, UPR, SR_*P, $UR_{\perp}C$, SPR, UPU,UCR, $(RC)_{\perp}U$, SP_*U,SC_*R, $(RR)_{\perp}C_{\perp}U$, $(RR)_{\perp}P_{\perp}S$, UPS, $UC_{\perp}U$
	4,5	$(RR)_{\perp}R_{\perp}R_{\perp}P$, $UR_{\perp}R_{\perp}P$, $(RR)_{\perp}R_{\perp}P_*R$, $(RR)_{\perp}R_{\perp}C$, $UR_{\perp}P_*R$, $(RR)_{\perp}P_*R_{\perp}R$, $(RC)_{\perp}R_{\perp}R$, $(RR)_{\perp}P_*U$, $(RR)_{\perp}C_{\perp}R$, $UP_*R_{\perp}R$, $UR_{\perp}P_*U$, SP_*R_*R, $(RR)_{\perp}P_{\perp}R_{\perp}U$, $UP_{\perp}R_{\perp}U$

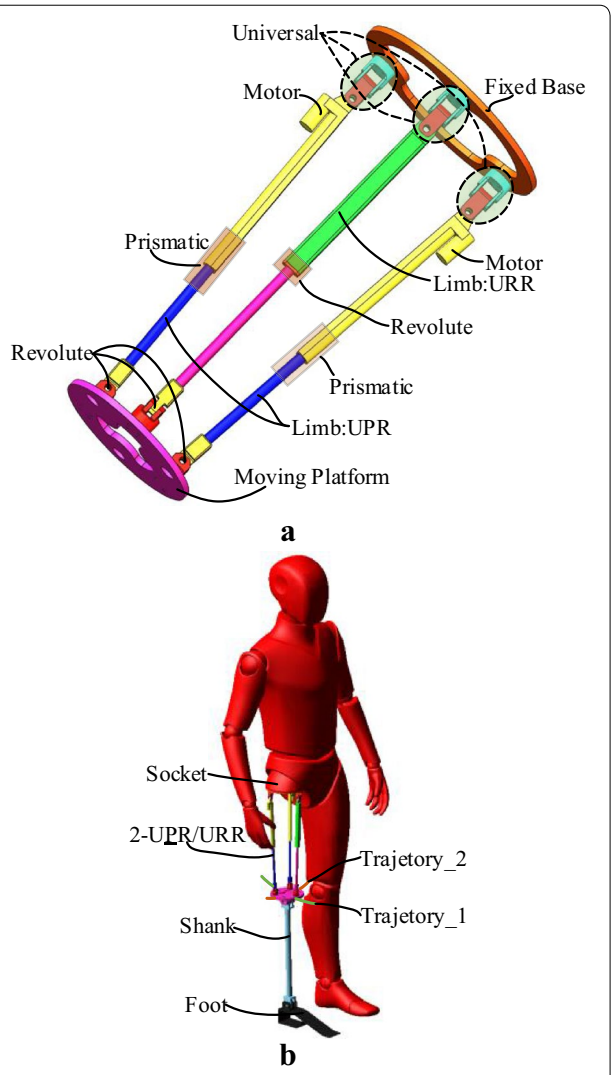

Figure 4 Hip prosthetic parallel mechanism: **a** 2-UPR/URR parallel mechanism; **b** amputee with hip prosthetic mechanism

$$\boldsymbol{a}_i + l_i \boldsymbol{s}_i = \boldsymbol{p} + \boldsymbol{b}_i, \tag{4}$$

where $\boldsymbol{s}_i$ is a unit vector pointing from A_i to B_i, l_i is the length of the ith limb, and is a constant when $i=1$. From Eqs. (3) and (4), the position vector of point o is solved:

$$\boldsymbol{p} = \begin{bmatrix} x_p \\ y_p \\ z_p \end{bmatrix} = \begin{bmatrix} l_1 \cos\alpha \sin\beta + \sqrt{3}a - b\cos\beta \\ l_1 \sin\alpha - b\sin\alpha\sin\beta \\ l_1 \cos\alpha\cos\beta + b\cos\alpha\sin\beta \end{bmatrix}^{\mathrm{T}}. \tag{5}$$

Therefore, the lengths l_i ($i=2$, 3) of limbs 2 and 3 are solved in terms of the value of α and β as follows:

$$l_i = \sqrt{(b_{ix} - a_{ix})^2 + (b_{iy} - a_{iy})^2 + (b_{iz} - a_{iz})^2}. \tag{6}$$

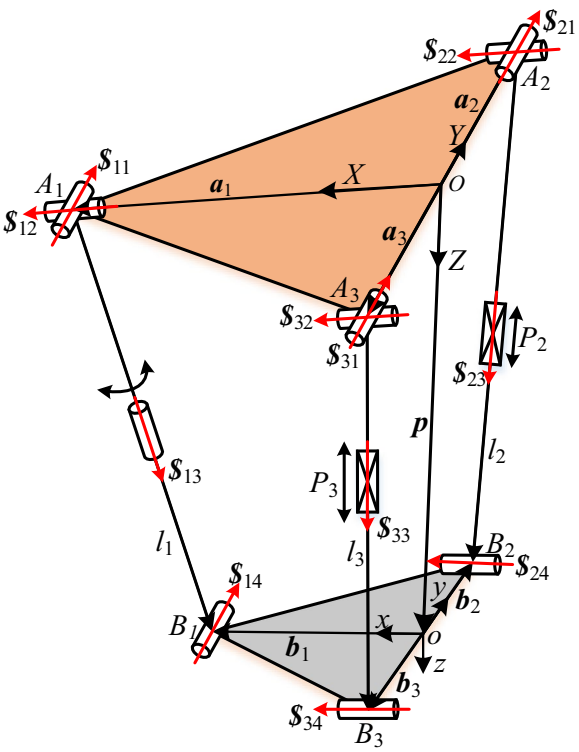

Figure 5 Diagram of 2-UPR/URR parallel mechanism

4 Jacobian Matrix

Based on the screw theory, the 6×6 fully Jacobian matrix [14–17] of the 2-UPR/URR parallel mechanism was constructed, which consisted of the constraint and kinematic Jacobian matrices.

4.1 Jacobian Matrix of UPR Limb

We assumed that the actuating limb UPR was an open-loop limb connecting the moving platform to the fixed base. The unit screw of the jth joint in the ith limb was expressed as $\$_{j,i}$, as shown in Figure 6. In order to facilitate the analysis, the origin of the instantaneous frame was defined at point o, and its x_s, y_s, and z_s axes were parallel to the X, Y, and Z axes, respectively.

Letting $\$_{\mathrm{d}} = [\boldsymbol{\omega}_n, \boldsymbol{v}_o]$ be the instantaneous kinematic screw of the moving platform, which can be expressed as a linear combination of the kinematic screws in the actuating limb, we have:

$$\$_d = \dot{\theta}_{4,i}\$_{4,i} + \dot{q}_i\$_{3,i} + \dot{\theta}_{2,i}\$_{2,i} + \dot{\theta}_{1,i}\$_{1,i} \tag{7}$$

In Eq. (7), $\dot{\theta}_{j,i}$ is the rotational angular velocity of the jth ($j=1$–4) joint in the ith ($i=2$,3) limb, and $\dot{q}_i$ is the linear velocity of prismatic in the ith limb.

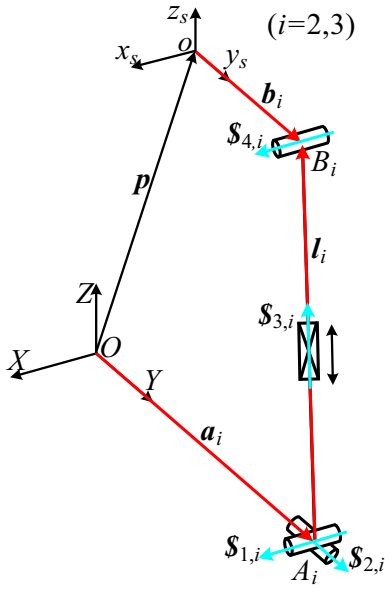

Figure 6 Actuating limb UPR

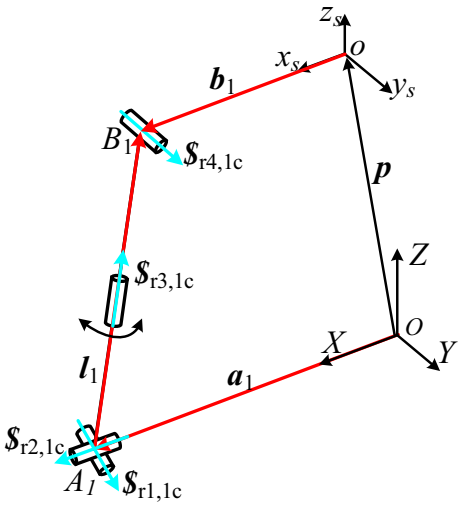

Figure 7 Passive limb URR

4.1.1 Constraint Jacobian Matrix

There were three passive joints and an actuating joint in the actuating limb, and its joint screws $\$_{j,i}$ (j=1–4, i=2, 3) were represented thusly:

$$\begin{cases} \$_{1,i} = \begin{bmatrix} \boldsymbol{s}_{1,i} & ({}^{B}\boldsymbol{b}_i - \boldsymbol{l}_i) \times \boldsymbol{s}_{1,i} \end{bmatrix}^{\mathrm{T}}, \\ \$_{2,i} = \begin{bmatrix} \boldsymbol{s}_{2,i} & ({}^{B}\boldsymbol{b}_i - \boldsymbol{l}_i) \times \boldsymbol{s}_{2,i} \end{bmatrix}^{\mathrm{T}}, \\ \$_{3,i} = \begin{bmatrix} 0 & \boldsymbol{s}_{3,i} \end{bmatrix}^{\mathrm{T}}, \\ \$_{4,i} = \begin{bmatrix} \boldsymbol{s}_{4,i} & {}^{B}\boldsymbol{b}_i \times \boldsymbol{s}_{4,i} \end{bmatrix}^{\mathrm{T}}. \end{cases} \tag{8}$$

The actuating limb was regarded as a spherical-revolute dyad that formed a four-screw system [18], so its constraint Jacobian matrix was composed of two constraint screws, which were reciprocal with the four-screw system:

$$\$_{r1,i} = \begin{bmatrix} \boldsymbol{s}_{1,i} \\ {}^{B}\boldsymbol{b}_i \times \boldsymbol{s}_{1,i} \end{bmatrix}, \quad \$_{r2,i} = \begin{bmatrix} \boldsymbol{s}_{3,i} \\ {}^{B}\boldsymbol{b}_i \times \boldsymbol{s}_{3,i} \end{bmatrix}. \tag{9}$$

Taking the dot-product of both sides of Eq. (7) with $\$_{r1,i}$ and $\$_{r2,i}$, the constraint Jacobian matrix of the two actuating limbs were obtained:

$$\boldsymbol{J}_{c2} = \begin{bmatrix} \boldsymbol{J}_{c21} \\ \boldsymbol{J}_{c22} \end{bmatrix} = \begin{bmatrix} ({}^{B}\boldsymbol{b}_2 \times \boldsymbol{s}_{4,2})^{\mathrm{T}} + \boldsymbol{s}_{2,2}^{\mathrm{T}} & \boldsymbol{s}_{4,2}^{\mathrm{T}} \\ ({}^{B}\boldsymbol{b}_3 \times \boldsymbol{s}_{4,3})^{\mathrm{T}} + \boldsymbol{s}_{2,3}^{\mathrm{T}} & \boldsymbol{s}_{4,3}^{\mathrm{T}} \end{bmatrix}, \tag{10}$$

where the row vector indicates that a constraint force and a constraint couple were imposed on the moving platform by each actuating limb.

4.1.2 Kinematic Jacobian Matrix

The actuating limbs became a universal-revolute dyad that formed a three-screw system [18] when the prismatic joint was locked. Compared with Eq. (8), a constraint screw was added:

$$\$_{r3,i} = \begin{bmatrix} \boldsymbol{s}_{3,i} \\ {}^{B}\boldsymbol{b}_i \times \boldsymbol{s}_{3,i} \end{bmatrix}, \quad i = 2,3. \tag{11}$$

The kinematic Jacobian matrices of the two actuating limbs were obtained by $\$_{r3,i}^{\mathrm{T}} \cdot \$_d = \dot{q}_i$:

$$\boldsymbol{J}_k = \begin{bmatrix} \boldsymbol{J}_{k1} \\ \boldsymbol{J}_{k2} \end{bmatrix} = \begin{bmatrix} ({}^{B}\boldsymbol{b}_2 \times \boldsymbol{s}_{3,2})^{\mathrm{T}} & \boldsymbol{s}_{3,2}^{\mathrm{T}} \\ ({}^{B}\boldsymbol{b}_3 \times \boldsymbol{s}_{3,3})^{\mathrm{T}} & \boldsymbol{s}_{3,3}^{\mathrm{T}} \end{bmatrix}. \tag{12}$$

4.2 Jacobian Matrix of the URR Limb

The unit screw of the jth joint was expressed as $\$_{j,1}$ for the passive limb URR, as shown in Figure 7.

The instantaneous kinematic characteristics of the moving platform can be expressed as a linear combination of the kinematic screws in the passive limb thusly:

$$\$_d = \dot{\theta}_{4,1}\$_{4,1} + \dot{\theta}_{3,1}\$_{3,1} + \dot{\theta}_{2,1}\$_{2,1} + \dot{\theta}_{1,1}\$_{1,1}. \tag{13}$$

In Eq. (13), $\dot{\theta}_{j,1}$ is the rotational angular velocity of the jth joint in Limb 1.

Since the passive limb had no actuator, it only contained a constraint Jacobian matrix, which acted as the constraint on the moving platform. The constraint Jacobian matrix of the passive limb could be obtained based on $\$_{r1,1}^{\mathrm{T}} \cdot \$_d = 0$ and $\$_{r2,1}^{\mathrm{T}} \cdot \$_d = 0$:

$$\boldsymbol{J}_{c1} = \begin{bmatrix} \boldsymbol{J}_{c11} \\ \boldsymbol{J}_{c12} \end{bmatrix} = \begin{bmatrix} ({}^{B}\boldsymbol{b}_1 \times \boldsymbol{s}_{1,1})^{\mathrm{T}} & \boldsymbol{s}_{1,1} \\ ({}^{B}\boldsymbol{b}_1 \times \boldsymbol{s}_{3,1})^{\mathrm{T}} & \boldsymbol{s}_{3,1} \end{bmatrix}. \tag{14}$$

In Eq. (14), the row vector indicates the constraint force on the moving platform imposed by the passive limb.

4.3 Fully Jacobian Matrix

According to the constraint Jacobian matrix and the kinematic Jacobian matrix, the fully Jacobian matrix of the 2-UPR/URR parallel mechanism could be obtained:

$$\boldsymbol{J} = \begin{bmatrix} \boldsymbol{J}_{c11} \\ \boldsymbol{J}_{c12} \\ \boldsymbol{J}_{c21} \\ \boldsymbol{J}_{c22} \\ \boldsymbol{J}_{k1} \\ \boldsymbol{J}_{k2} \end{bmatrix} = \begin{bmatrix} ({}^{B}\boldsymbol{b}_1 \times \boldsymbol{s}_{1,1})^{\mathrm{T}} & \boldsymbol{s}_{1,1}^{\mathrm{T}} \\ ({}^{B}\boldsymbol{b}_1 \times \boldsymbol{s}_{3,1})^{\mathrm{T}} & \boldsymbol{s}_{3,1}^{\mathrm{T}} \\ ({}^{B}\boldsymbol{b}_2 \times \boldsymbol{s}_{4,2})^{\mathrm{T}} + \boldsymbol{s}_{2,2}^{\mathrm{T}} & \boldsymbol{s}_{4,2}^{\mathrm{T}} \\ ({}^{B}\boldsymbol{b}_3 \times \boldsymbol{s}_{4,3})^{\mathrm{T}} + \boldsymbol{s}_{2,3}^{\mathrm{T}} & \boldsymbol{s}_{4,3}^{\mathrm{T}} \\ ({}^{B}\boldsymbol{b}_2 \times \boldsymbol{s}_{3,2})^{\mathrm{T}} & \boldsymbol{s}_{3,2}^{\mathrm{T}} \\ ({}^{B}\boldsymbol{b}_3 \times \boldsymbol{s}_{3,3})^{\mathrm{T}} & \boldsymbol{s}_{3,3}^{\mathrm{T}} \end{bmatrix}. \tag{15}$$

5 Performance Analysis

5.1 Workspace

In order to guarantee the rotation of the 2-UPR/URR parallel mechanism around the *X*-axis and *Y*-axis, which could meet the rotational angle of the hip in multiple gait modes, its workspace [19] was analyzed.

The geometry size of the amputee's thigh was measured: $l_1 = 310$, $a_1 = 105$, $a_2 = a_3 = 60$, $b_1 = 70$, $b_2 = b_3 = 40$. Thus, the workspace of the mechanism was solved, as shown in Figure 8.

Figure 8 shows that the mechanism had a large workspace and rotational angle around the *X*-axis and *Y*-axis, which exceeded the required ultimate rotational angle in multiple gait modes. The shape and position of the workspace were in accord with the movement of the human hip. When the moving platform rotated around the *X*-axis, $\alpha = [-60°, 60°]$, the moving range of the moving platform along the *Y*-axis was [−80 mm, 80 mm], as shown in Figure 8(a). When it rotated around the *Y*-axis, $\beta = [-90°, 35°]$, the moving range along the *X*-axis was [−40 mm, 160 mm], as shown in Figure 8(b). This also indicated that the mechanism was feasible when applied as a hip prosthetic mechanism, and confirmed the correctness of the fully Jacobian matrix.

5.2 Stiffness

In order to verify the influence of a passive limb on the stiffness of the parallel mechanism, the stiffness was analyzed in this paper for the 2-UPR parallel mechanism and the 2-UPR/URR parallel mechanism with the passive limb.

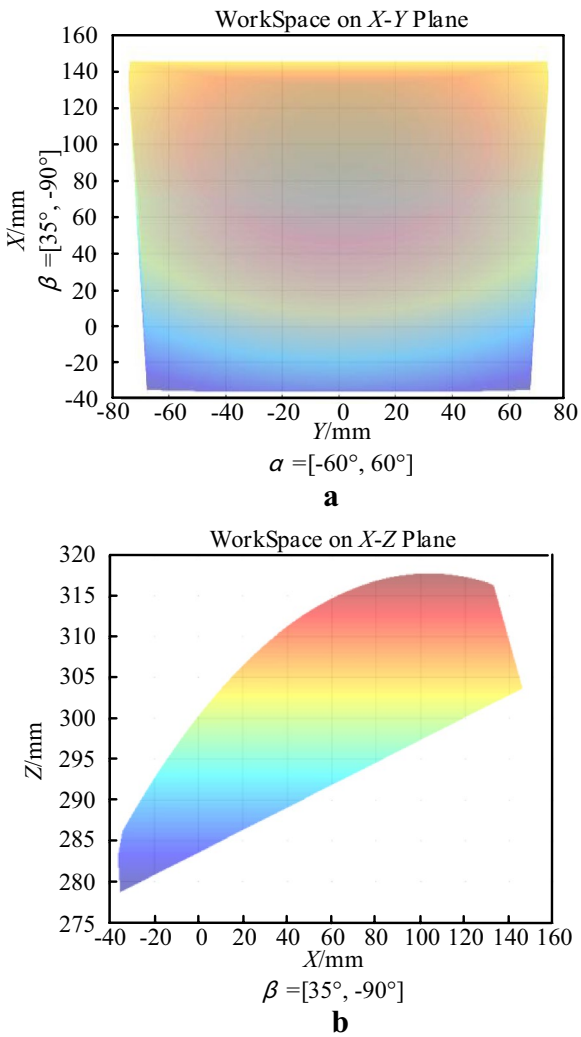

Figure 8 Workspace of the 2-UPR/URR Parallel Mechanism: **a** spatial location on the *X-Y* plane; **b** spatial location on the *X-Z* plane

Assuming that the moving platform was subjected to an external force $\boldsymbol{F}_{\mathrm{e}} = [\boldsymbol{f}_{\mathrm{e}}, \boldsymbol{n}_{\mathrm{e}}]^{\mathrm{T}}$, and the frictional force at the joints was ignored. The stiffness and structural deformation [20] could thus be solved when loaded:

$$K = k\boldsymbol{J}^{\mathrm{T}}J, \tag{16a}$$

$$\boldsymbol{F}_{\mathrm{e}} = \boldsymbol{K} \cdot \Delta\boldsymbol{x}. \tag{16b}$$

In Eq. (16), $\boldsymbol{F}_{\mathrm{e}}$ is the external force exerted on the moving platform, $\Delta\boldsymbol{x}$ is the deformation displacement of the moving platform under external force, $\boldsymbol{K}$ is the stiffness matrix, and k is the equivalent spring constant assuming $k = 1000$ N/mm via the material properties in Ref. [21].

The complete gait cycle was composed of the single and double support stages, all of which bore the weight of the

trunk. Therefore, the prosthetic mechanism required sufficient stiffness. The fully Jacobian matrices of the stiffness distribution of the 2-UPR parallel mechanism and 2-UPR/URR parallel mechanism were obtained, as shown in Figure 9.

In Figure 9, the maximum stiffness of the 2-UPR parallel mechanism was about 2853 N/mm within $\alpha = -25°$ to approximately 25°, $\beta = 0°$ to approximately 30°, and the maximum stiffness of the 2-UPR/URR parallel mechanism was 4435 N/mm within $\alpha = -25°$ to approximately 25° and $\beta = -90°$ to approximately $-60°$. These results indicated that the stiffness of the parallel mechanism had been improved by introducing a passive limb. In addition, due to the presence of the passive limb, the stiffness of the 2-UPR/URR parallel mechanism was still higher at the ultimate position during flexion, as shown in Figure 9(b).

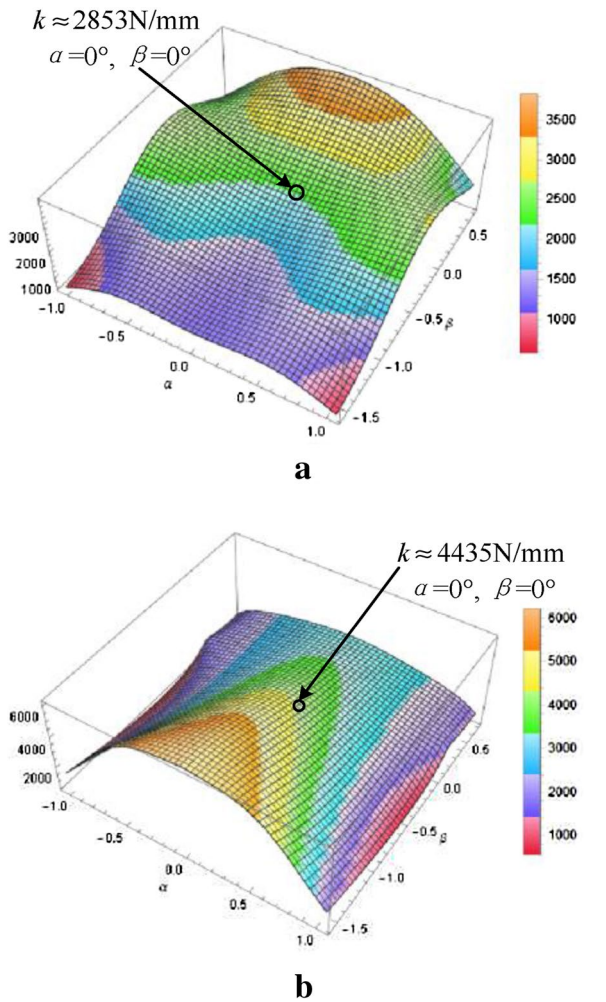

Figure 9 Stiffness distribution of the mechanism in the single support phase: **a** 2-UPR parallel mechanism; **b** 2-UPR/ URR parallel mechanism

In order to verify the theoretical solution of the stiffness of the 2-UPR/URR parallel mechanism, static analysis was carried out based on the finite element method. Clearly, the hip prosthetic mechanism exerted a maximum weight when it was a supporting leg in the single support phase. The total gravity was a concentrated force, including a load of 20 kg, which was about 1000 N. It was exerted on the center of the moving platform, in a vertically downward direction. The deformation of the mechanism could then be solved by OptiStruct, as shown in Figure 10.

In Figure 10, the maximum deformation of the 2-UPR/URR parallel mechanism was about 0.2315 mm, and the stiffness of the mechanism was 3455.72 N/mm, which could be calculated by Eq. (16b). The simulation result of the 2-UPR/URR parallel mechanism was about 979 N/mm less than the theoretical solution when $\alpha = \beta = 0°$. The results indicated that the mechanism had sufficient stiffness to resist maximum external load in a single support phase without a large deformation.

5.3 Buckling Analysis

Since the axial length of the parallel prosthetic mechanism was much larger than its radial length, in order to predict the maximum loading capacity and avoid the instability and collapse caused by the external load, its buckling analysis was necessary. Generally, the buckling analysis of the mechanism is based on its eigenvalue problem:

$$(\boldsymbol{K} - \lambda_\sigma \boldsymbol{K}_\sigma)\boldsymbol{\varphi} = 0. \tag{17}$$

In Eq. (17), $\boldsymbol{K}$ is the structural stiffness matrix, λ_σ is the scale multiplier for the external load, also called the eigenvalue, $\boldsymbol{K}_\sigma$ is the geometric stiffness matrix based on

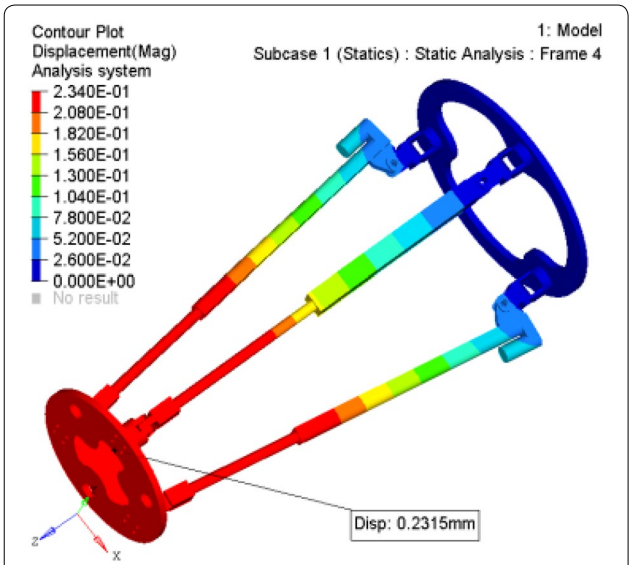

Figure 10 Deformation under external load (mm)

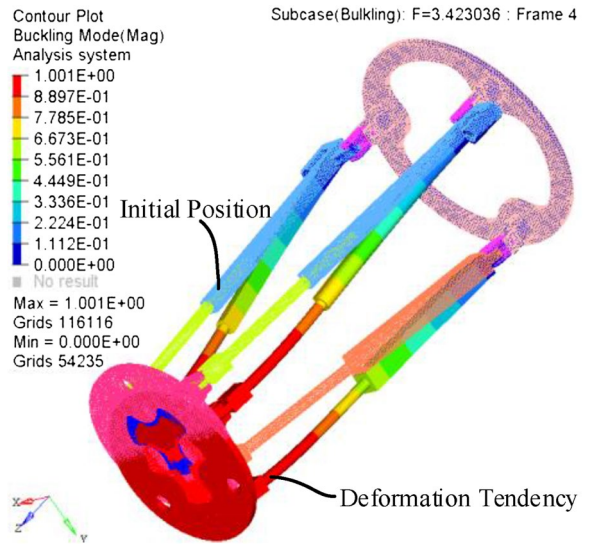

Figure 11 Result of the buckling analysis of the mechanism (mm)

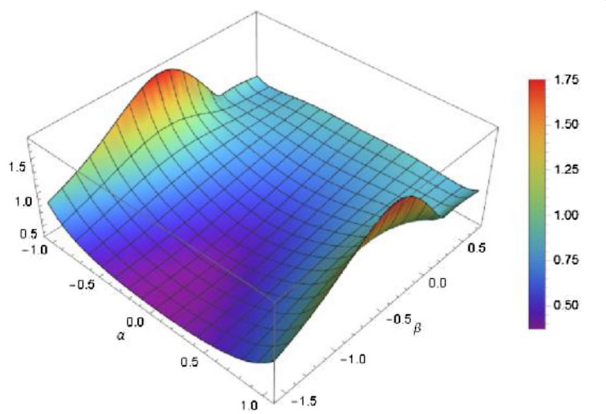

Figure 12 Dexterity based on the Jacobian condition number

the static analysis result, and $\boldsymbol{\phi}$ is the eigenvector. The eigenvalue λ_σ in Eq. (17) is solved by the Lanczos method [22]. Thus, the critical load that the mechanism can bear without instability is solved:

$$f_\sigma = \lambda_\sigma f_e. \tag{18}$$

According to Eq. (17) and the static analysis result, the critical load and large deformation trend of the mechanism were obtained in a critical unstable state, as shown in Figure 11.

Furthermore, the scaling factor of the external load was $\lambda_\sigma \approx 1.72$, which was calculated from the buckling analysis, and the critical load for the mechanism instability was $f_\sigma = 1376$ N in terms of Eq. (18). As the weight of the amputee patient, 80 kg, was less than the critical load f_σ, the amputee could also bear an additional weight of 57.6 kg without instability while the 2-UPR/URR parallel mechanism served as the hip prosthetic mechanism.

5.4 Dexterity

In this paper, in terms of the fully Jacobian matrix of the 2-UPR/URR parallel mechanism expressed in Eq. (15), its condition number [23–25] index was analyzed as follows:

$$\kappa(\boldsymbol{J}) = \frac{\sigma_{\max}}{\sigma_{\min}}, \tag{19}$$

where $\kappa(\boldsymbol{J})$ is the condition number, $\sigma_{\max}$ is the maximum eigenvalue of the Jacobian matrix, and $\sigma_{\min}$ is the minimum eigenvalue of the inverse Jacobian matrix.

According to the geometry size in Section 5.1, the dexterity map of the 2-UPR/URR parallel mechanism is shown in Figure 12.

Compared with the motion characteristics of the hip in Table 1, the rotational angles of the 2-UPR/URR parallel mechanism around the X-axis and Y-axis were larger. The condition number of the 2-UPR/URR parallel mechanism as 0 to approximately 1 when the moving platform was within the range $-50°$ to approximately 50° around the X-axis and $-90°$ to approximately 40° around the Y-axis, which indicated the kinematic dexterity of the mechanism was good.

In addition, the condition number of the mechanism was close to 1 when the moving platform rotated to 45° around the X-axis or within the range of 0° to approximately 40° around the Y-axis, which indicated the position was isotropic and had an optimal kinematic performance in this area. Since no singularity occurred, relative analysis was not necessary. Results showed that the 2-UPR/URR parallel mechanism was feasible and in accord with the design requirements for a hip prosthetic mechanism.

6 Dynamic Model of 2-UPR/URR Parallel Mechanism

6.1 Velocity and Acceleration of Actuating Limbs

To facilitate the inverse dynamic analysis [18, 26–29], a local coordinate system o_i-$x_iy_iz_i$ was built in the vertex A_i of the fixed base, which represented the orientation of limb i with respect to the fixed frame, as shown in Figure 13. The unit vector expressed in the ith limb frame was ${}^i\boldsymbol{s}_i = [0,\ 0,\ 1]^{\mathrm{T}}$, which represented the direction of the z_i axis. The o_i-$x_iy_iz_i$ could be defined as a rotation of η_i about the x_i axis, followed by a second rotation of χ_i around y_i':

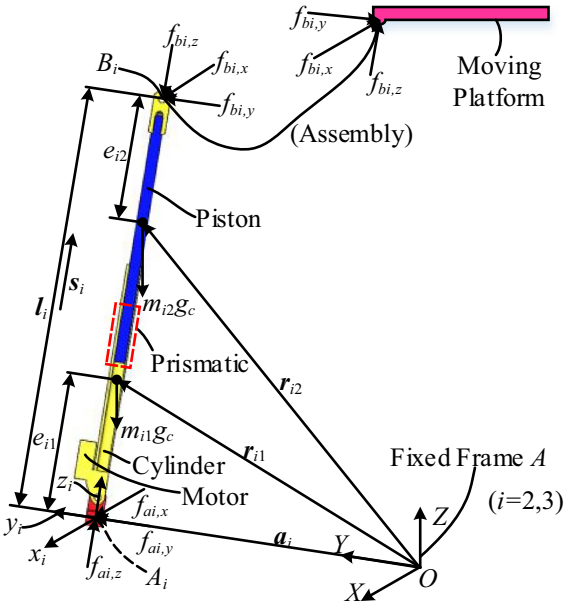

Figure 13 Free-body diagram of the *i*th actuating limb

$$ {}^{A}\boldsymbol{R}_i = \begin{bmatrix} c\eta_i c\chi_i & -s\eta_i & c\eta_i s\chi_i \\ s\eta_i c\chi_i & c\eta_i & s\eta_i s\chi_i \\ -s\chi_i & 0 & c\chi_i \end{bmatrix}, \tag{20} $$

where s is the represented sine function, and c is the represented cosine function.

The ith (i=2, 3) driving limb of the mechanism consisted of a cylinder and a piston, as shown in Figure 13. Letting e_{i1} be the distance between A_i and the center of mass of the ith cylinder, and letting e_{i2} be the distance between B_i and the center of the mass of the ith piston, then the position vector of the centers of mass of the ith cylinder and piston could be represented thusly:

$$ \begin{cases} \boldsymbol{r}_{i1} = \boldsymbol{a}_i + e_{i1}\boldsymbol{s}_i, \\ \boldsymbol{r}_{i2} = \boldsymbol{a}_i + (l_i - e_{i2})\boldsymbol{s}_i. \end{cases} \tag{21} $$

6.1.1 Velocity Analysis

Taking the time derivative of the right-hand side of Eq. (4), the velocity of the vertex B_i, defined as $\boldsymbol{v}_{bi}$, is solved:

$$ \boldsymbol{v}_{bi} = \boldsymbol{v}_p + \boldsymbol{\omega}_p \times \boldsymbol{b}_i, \tag{22} $$

where $\boldsymbol{v}_p$ and $\boldsymbol{\omega}_p$ are, respectively, the linear velocity and angular velocity of the moving platform expressed in the fixed frame, which can be solved by Eqs. (3) and (4).

Based on ${}^{A}\boldsymbol{R}_i$ and Eq. (22), the velocity of the vertex B_i is ${}^{i}\boldsymbol{v}_{bi}$=[${}^{i}\boldsymbol{v}_{bix}$, ${}^{i}\boldsymbol{v}_{biy}$, ${}^{i}\boldsymbol{v}_{biz}$], which could be obtained thusly:

$$ {}^{i}\boldsymbol{v}_{bi} = {}^{i}\boldsymbol{R}_A \boldsymbol{v}_{bi} = l_i {}^{i}\boldsymbol{\omega}_i \times {}^{i}\boldsymbol{s}_i + \dot{l}_i {}^{i}\boldsymbol{s}_i \tag{23} $$

as the actuating limb cannot rotate about the z_i axis. Dot-multiplying and cross-multiplying both sides of Eq. (23) by ${}^{i}\boldsymbol{s}_i$, the linear and angular velocities of the ith actuating limb could be calculated:

$$ \begin{cases} \dot{l}_i = {}^{i}\boldsymbol{s}_i {}^{i}\boldsymbol{\upsilon}_{bi} = {}^{i}v_{biz}, \\ {}^{i}\boldsymbol{\omega}_i = ({}^{i}\boldsymbol{s}_i \times {}^{i}\boldsymbol{v}_{bi})/l_i = [-{}^{i}v_{biy}, -{}^{i}v_{bix}, 0]^{\mathrm{T}}/l_i. \end{cases} \tag{24} $$

The velocities of the centers of mass of the ith cylinder and piston could be calculated by differentiating Eqs. (21) with respect to time and combining with Eq. (24):

$$ \begin{cases} {}^{i}\boldsymbol{v}_{i1} = e_{i1} {}^{i}\boldsymbol{\omega}_i \times {}^{i}\boldsymbol{s}_i, \\ {}^{i}\boldsymbol{v}_{i2} = (l_i - e_{i2}) {}^{i}\boldsymbol{\omega}_i \times {}^{i}\boldsymbol{s}_i + \dot{l}_i {}^{i}\boldsymbol{s}_i. \end{cases} \tag{25} $$

6.1.2 Acceleration Analysis

Based on the acceleration synthesis theorem [27], the acceleration of the vertex B_i, ${}^{i}\boldsymbol{a}_{bi}$, was found by differentiating Eq. (23) with respect to time:

$$ \begin{aligned} {}^{i}\boldsymbol{a}_{bi} = {}^{i}\dot{\boldsymbol{v}}_{bi} = \ddot{l}_i {}^{i}\boldsymbol{s}_i + l_i {}^{i}\dot{\boldsymbol{\omega}}_i \times {}^{i}\boldsymbol{s}_i + \cdots \\ + l_i {}^{i}\boldsymbol{\omega}_i \times ({}^{i}\boldsymbol{\omega}_i \times {}^{i}\boldsymbol{s}_i) + 2\dot{l}_i {}^{i}\boldsymbol{\omega}_i \times {}^{i}\boldsymbol{s}_i \end{aligned} \tag{26} $$

as each actuating limb cannot spin about its own axis. Dot-multiplying and cross-multiplying both sides of Eq. (26) by ${}^{i}\boldsymbol{s}_i$, we obtained the linear and angular velocities of the ith actuating limb:

$$ \begin{cases} \ddot{l}_i = {}^{i}\boldsymbol{s}_i {}^{i}\dot{\boldsymbol{v}}_{bi} + l_i {}^{i}\boldsymbol{\omega}_i^2, \\ {}^{i}\dot{\boldsymbol{\omega}}_i = ({}^{i}\boldsymbol{s}_i \times {}^{i}\dot{\boldsymbol{v}}_{bi} - 2\dot{l}_i {}^{i}\boldsymbol{\omega}_i)/l_i. \end{cases} \tag{27} $$

The acceleration of the centers of mass of the ith cylinder and piston could be solved by differentiating Eq. (25) with respect to time and combining with Eq. (27):

$$ \begin{cases} {}^{i}\boldsymbol{a}_{i1} = e_{i1} {}^{i}\dot{\boldsymbol{\omega}}_i \times {}^{i}\boldsymbol{s}_i + e_{i1} {}^{i}\boldsymbol{\omega}_i \times ({}^{i}\boldsymbol{\omega}_i \times {}^{i}\boldsymbol{s}_i), \\ {}^{i}\boldsymbol{a}_{i2} = (l_i - e_{i2}) {}^{i}\dot{\boldsymbol{\omega}}_i \times {}^{i}\boldsymbol{s}_i + (l_i - e_{i2}) {}^{i}\boldsymbol{\omega}_i \cdots \\ \qquad \times ({}^{i}\boldsymbol{\omega}_i \times {}^{i}\boldsymbol{s}_i) + 2\dot{l}_i {}^{i}\boldsymbol{\omega}_i \times {}^{i}\boldsymbol{s}_i + \ddot{l}_i {}^{i}\boldsymbol{s}_i. \end{cases} \tag{28} $$

6.2 Velocity and Acceleration of Passive Limbs

6.2.1 Velocity Analysis

The passive limb of the 2-UPR/URR parallel mechanism consisted of an upper rod and a lower rod, as shown in Figure 14.

Letting e_{11} be the distance between A_1 and the center of the mass of the lower rod, and letting e_{12} be the distance between B_1 and the center of mass of the upper rod, as shown in Figure 14, the position vector of the centers of mass of the lower and upper rods could be represented as:

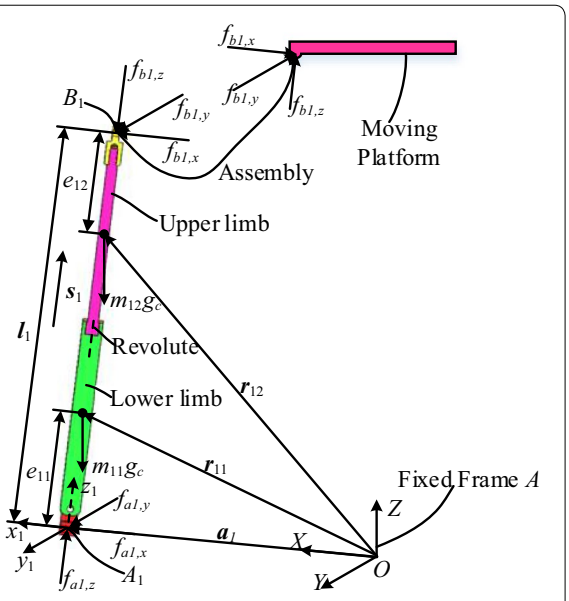

Figure 14 Free-body diagram of passive limb

$$\begin{cases} \boldsymbol{r}_{11} = \boldsymbol{a}_1 + e_{11}\boldsymbol{s}_1, \\ \boldsymbol{r}_{12} = \boldsymbol{a}_1 + (l_1 - e_{12})\boldsymbol{s}_1. \end{cases} \tag{29}$$

As the passive limb cannot move along the z_1 axis, the linear and angular velocities of the vertex B_1 were obtained based on ${}^{A}\boldsymbol{R}_1$ and Eq. (22):

$$\begin{cases} {}^{1}\boldsymbol{v}_{b1} = [{}^{1}v_{b1x}, {}^{1}v_{b1y}, {}^{1}v_{b1z}] = l_1 {}^{1}\boldsymbol{\omega}_1 \times {}^{1}\boldsymbol{s}_1, \\ {}^{1}\boldsymbol{\omega}_1 = \frac{1}{l_1}({}^{1}\boldsymbol{s}_1 \times {}^{1}\boldsymbol{v}_{b1}) = \frac{1}{l_1}[-{}^{1}v_{b1y}, -{}^{1}v_{b1x}, 0]. \end{cases} \tag{30}$$

Therefore, the velocities of the center of the mass of the lower and upper rods are expressed as:

$$\begin{cases} {}^{1}\boldsymbol{v}_{11} = e_{11} {}^{1}\boldsymbol{\omega}_1 \times {}^{1}\boldsymbol{s}_1, \\ {}^{1}\boldsymbol{v}_{12} = (l_1 - e_{11}) {}^{1}\boldsymbol{\omega}_1 \times {}^{1}\boldsymbol{s}_1. \end{cases} \tag{31}$$

6.2.2 Acceleration Analysis

The acceleration of B_1, expressed in its limb frame, was found by differentiating Eq. (31) with respect to time:

$${}^{1}\boldsymbol{a}_{b1} = {}^{1}\dot{\boldsymbol{v}}_{b1} = l_1 {}^{1}\dot{\boldsymbol{\omega}}_1 \times {}^{1}\boldsymbol{s}_1 + l_1 {}^{1}\boldsymbol{\omega}_1 \times ({}^{1}\boldsymbol{\omega}_1 \times {}^{1}\boldsymbol{s}_1). \tag{32}$$

Cross-multiplying both sides of Eq.(32) by ${}^{1}\boldsymbol{s}_1$, the angular acceleration of the passive limb can be calculated:

$${}^{1}\dot{\boldsymbol{\omega}}_1 = ({}^{1}\boldsymbol{s}_1 \times {}^{1}\dot{\boldsymbol{v}}_{b1})/l_1. \tag{33}$$

The acceleration of the center of mass of the lower and upper rods of the passive limb are then expressed as:

$$\begin{cases} {}^{i}\dot{\boldsymbol{v}}_{i1} = e_{11} {}^{1}\dot{\boldsymbol{\omega}}_1 \times {}^{1}\boldsymbol{s}_1 + e_{11} {}^{1}\boldsymbol{\omega}_1 \times ({}^{1}\boldsymbol{\omega}_1 \times {}^{1}\boldsymbol{s}_1), \\ {}^{i}\dot{\boldsymbol{v}}_{i2} = (l_1 - e_{12}) {}^{1}\dot{\boldsymbol{\omega}}_1 \times {}^{1}\boldsymbol{s}_1 + (l_1 - e_{12}) {}^{1}\boldsymbol{\omega}_1 \times ({}^{1}\boldsymbol{\omega}_1 \times {}^{1}\boldsymbol{s}_1). \end{cases} \tag{34}$$

6.3 Jacobian Matrix of Mechanism

6.3.1 Jacobian Matrix of the Moving Platform

In this paper, the virtual work principle was adopted to solve the dynamic solution of the mechanism. Hence, a critical step in building the dynamic equations of the mechanism was the construction of the Jacobian matrix of the moving platform and the link Jacobian matrices.

Based on Eq. (24) in matrix form, the Jacobian matrix of the moving platform could be obtained:

$$\begin{bmatrix} \dot{l}_2 \\ \dot{l}_3 \end{bmatrix} = \begin{bmatrix} {}^{2}\boldsymbol{J}_{b2z} \\ {}^{3}\boldsymbol{J}_{b3z} \end{bmatrix}_{2\times 6} \cdot \dot{\boldsymbol{x}}_p = \boldsymbol{J}_p \dot{\boldsymbol{x}}_p, \tag{35}$$

where $\boldsymbol{J}_p = [{}^{2}\boldsymbol{J}_{b2z}, {}^{3}\boldsymbol{J}_{b3z}]^{\mathrm{T}}$ is the Jacobian matrix of the moving platform, which is expressed as the velocity mapping relationship among all actuators and the moving platform.

6.3.2 Link Jacobian Matrices

Combining Eqs. (24), (25), (30) and (31), the link Jacobian matrices could be obtained:

$$\begin{cases} {}^{i}\dot{\boldsymbol{x}}_{i1} = {}^{i}\boldsymbol{J}_{i1}\dot{\boldsymbol{x}}_p = [{}^{i}\boldsymbol{v}_{i1}, {}^{i}\boldsymbol{\omega}_i]^{\mathrm{T}}\dot{\boldsymbol{x}}_p, \\ {}^{i}\dot{\boldsymbol{x}}_{i2} = {}^{i}\boldsymbol{J}_{i2}\dot{\boldsymbol{x}}_p = [{}^{i}\boldsymbol{v}_{i2}, {}^{i}\boldsymbol{\omega}_i]^{\mathrm{T}}\dot{\boldsymbol{x}}_p, \end{cases} \tag{36}$$

where ${}^{i}\dot{\boldsymbol{x}}_{i1}$ and ${}^{i}\dot{\boldsymbol{x}}_{i2}$ are the velocities of the center of mass of the upper rod and lower rod in the passive limb when $i=1$, and denotes the velocities of the center of mass of the cylinder and piston in the ith actuating limb when $i=2, 3$. $\dot{\boldsymbol{x}}_p$ denotes the velocity of the moving platform. ${}^{i}\boldsymbol{J}_{i1}$ and ${}^{i}\boldsymbol{J}_{i2}$ are the link Jacobian matrices, respectively, of the cylinder and piston in the ith actuating limb.

6.4 Dynamic Equations

6.4.1 Inertia and Applied Wrenches

The vector sum of applied and inertia wrenches is denoted as $\boldsymbol{F}_p = [\boldsymbol{f}_p, \boldsymbol{n}_p]^{\mathrm{T}}$, which is exerted at the center of mass of the moving platform of the 2-UPR/URR parallel mechanism:

$$\boldsymbol{F}_p = \begin{bmatrix} \boldsymbol{f}_p \\ \boldsymbol{n}_p \end{bmatrix} = \begin{bmatrix} \boldsymbol{f}_e + m_p\boldsymbol{g} - m_p\boldsymbol{a}_p \\ \boldsymbol{n}_e - {}^{A}\boldsymbol{I}_p\dot{\boldsymbol{\omega}}_p - \boldsymbol{\omega}_p \times ({}^{A}\boldsymbol{I}_p\boldsymbol{\omega}_p) \end{bmatrix}, \tag{37}$$

where $\boldsymbol{F}_e = [\boldsymbol{f}_e, \boldsymbol{n}_e]$ is the resultant force vector acted on the center of mass of the moving platform. m_p is the mass of the moving platform, ${}^{B}\boldsymbol{I}_p$ is the inertia matrix of the moving platform, ${}^{A}\boldsymbol{I}_p$ denotes the inertia matrix of the moving platform, and ${}^{A}\boldsymbol{I}_p = {}^{A}\boldsymbol{R}_B \, {}^{B}\boldsymbol{I}_P \, {}^{B}\boldsymbol{R}_A$.

Similarly, ${}^{i}\boldsymbol{F}_{i1}$ and ${}^{i}\boldsymbol{F}_{i2}$ are the vector sum of applied and inertia wrenches exerted at the centers of mass of the

lower and upper rods when $i=1$. They are the vector sum of applied and inertia wrenches exerted at the centers of the mass of the cylinder and piston when $i=2, 3$:

$$\begin{cases} {}^{i}\boldsymbol{F}_{i1} = \begin{bmatrix} m_{i1}{}^{i}\boldsymbol{R}_{A}\boldsymbol{g} - m_{i1}{}^{i}\boldsymbol{a}_{i1} \\ -{}^{i}\boldsymbol{I}_{i1}{}^{i}\dot{\boldsymbol{\omega}}_{i} - {}^{i}\boldsymbol{\omega}_{i} \times ({}^{i}\boldsymbol{I}_{i1}{}^{i}\boldsymbol{\omega}_{i}) \end{bmatrix}, \\ {}^{i}\boldsymbol{F}_{i2} = \begin{bmatrix} m_{i2}{}^{i}\boldsymbol{R}_{A}\boldsymbol{g} - m_{i2}{}^{i}\boldsymbol{a}_{i2} \\ -{}^{i}\boldsymbol{I}_{i2}{}^{i}\dot{\boldsymbol{\omega}}_{i} - {}^{i}\boldsymbol{\omega}_{i} \times ({}^{i}\boldsymbol{I}_{i2}{}^{i}\boldsymbol{\omega}_{i}) \end{bmatrix}, \end{cases} \tag{38}$$

where ${}^{i}m_{i1}$ and ${}^{i}m_{i2}$ are, respectively, the mass of the lower rod and upper rod when $i=1$. They are the mass of the cylinder and piston when $i=2, 3$. ${}^{i}\boldsymbol{I}_{i1}$ and ${}^{i}\boldsymbol{I}_{i2}$ denote, respectively, the inertia matrix of the lower rod and the upper rod in the ith limb.

6.4.2 Dynamic Equations

From the above, the dynamic model was established based on the virtual work principle [20,30] as follows:

$$\boldsymbol{J}_{p}^{\mathrm{T}}\boldsymbol{\tau} + \boldsymbol{F}_{p} + \sum_{i=1}^{3}({}^{i}\boldsymbol{J}_{i1}^{\mathrm{T}}{}^{i}\boldsymbol{F}_{i1} + {}^{i}\boldsymbol{J}_{i2}^{\mathrm{T}}{}^{i}\boldsymbol{F}_{i2}) = 0. \tag{39}$$

To facilitate the calculation, substituting Eqs. (37) and (38) into Eq. (39) and simplifying yields:

$$\boldsymbol{J}_{p}^{\mathrm{T}}\boldsymbol{\tau} + \boldsymbol{F}_{p} + \sum_{i=1}^{3}(\boldsymbol{J}_{x}^{\mathrm{T}}\boldsymbol{F}_{x} + \boldsymbol{J}_{y}^{\mathrm{T}}\boldsymbol{F}_{y}) = 0, \tag{40}$$

where $\boldsymbol{\tau} = [0, \tau_2, \tau_3]$ is the vector of actuator forces, which is specified in the actuator.

7 Numerical Verification

The material properties of all parts of the mechanism are shown in Table 4.

The mass of each component was $m_{\mathrm{p}}=1.5$ kg, $m_{11}=0.9$ kg, $m_{12}=0.75$ kg, $m_{i1}=1.2$ kg, and $m_{i2}=0.75$ kg. In terms of Ref. [21], the inertia matrix $\boldsymbol{I}_p$ and ${}^{i}\boldsymbol{I}_{i}$ $(i=1, 2, 3)$ could be obtained:

$$I_p = \begin{bmatrix} 0.348 & 0 & 0 \\ 0 & 0.174 & 0 \\ 0 & 0 & 0.174 \end{bmatrix}, \quad {}^{i}I_i = \begin{bmatrix} 0.316 & 0 & 0 \\ 0 & 0.296 & 0 \\ 0 & 0 & 0 \end{bmatrix}, \tag{41}$$

Table 4 Material property parameters

Attribute	Numerical value
Material	Steel
Young modulus E (N/mm^2)	2.1×10^{-5}
Poisson's ratio μ	0.3
Density ρ (t/mm^3)	7.9×10^{-9}

where the unit of inertia is kg/m^2, and the gravity is $g=[0, 0, -9807]^{\mathrm{T}}$ mm/s^2.

Moreover, the joint forces were tested using the force-measuring platform in a gait cycle, which was defined as $\boldsymbol{F}_{\mathrm{e}}$. It was obtained by the equivalent method:

1) $\boldsymbol{F}_{\mathrm{e}}=[-20, 0, 25, 30, 30, 0]$, for the human without load.
2) $\boldsymbol{F}_{\mathrm{e}}=[-35, 0, 50, 60, 50, 0]$, for the human with a load of 20 kg.

Based on these equations, the dynamic problem of the 2-UPR/URR parallel mechanism was programmed and calculated by Mathematica, which was verified by the simulation results.

7.1 Dynamic Verification

According to the gait testing in Section 2, the motion curves of the hip in four gait modes were obtained by using MotionAnalysis, as shown in Figure 15. The hip motion trajectories were all approximate during flexion and extension, though the ultimate rotational angles were different. However, the hip motion trajectories were nearly similar during abduction and adduction.

Therefore, the dynamics of the prosthetic mechanism was mainly analyzed in two gait modes based on Figure 15:

1) First mode: the velocity was 3.0 m/s with a load of 20 kg during flexion and extension.
2) Second mode: the velocity was 1.5 m/s without loading during abduction and adduction.

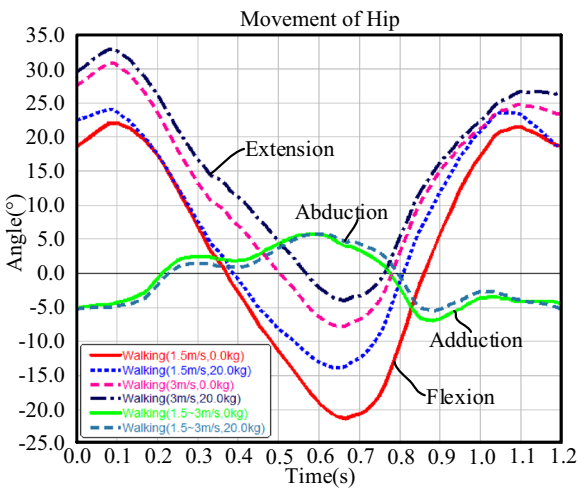

Figure 15 Motion angles for the hip in multiple gait modes

Furthermore, based on the human dynamic analysis, the flexion and extension of the hip prosthetic parallel mechanism in the gait cycle, as shown in Figure 16. As can be seen in Figure 16, the human gait cycle could be divided into five phases in terms of kinesiology [11].

The motions of the hip prosthetic parallel mechanism in the five phases are summarized, as shown in Table 5.

By the curve fitting method, the motion trajectory of the moving platform could be derived in the first gait mode, as shown in Eq. (42):

$$\begin{cases} \alpha = 0, \\ \beta = \begin{cases} \frac{35\pi}{18}t^2 + \frac{59\pi}{360}, & 0 \le t < 0.1, \\ \frac{11\pi}{60}\cos\left(\frac{20\pi}{11}t - \frac{2\pi}{11}\right) + \frac{7\pi}{72}, & 0.1 \le t < 1.1, \\ -\frac{\pi}{36}t + \frac{13\pi}{72}, & 1.1 \le t < 1.2. \end{cases} \end{cases} \tag{42}$$

The ith ($i=2,3$) actuating forces versus time calculated by the program showed in Figure 17(a), and the simulation results based on Adams are plotted in Figure 17(b).

Results showed that the theoretical solution was the same, owing to the symmetrical arrangement of the actuating limbs. However, the actuating forces were highly approximated in the simulation environment, and the error may have been caused by the rigid connection of the kinematic pairs.

By the curve fitting method, the motion trajectory of the moving platform could be obtained in the second gait mode, as shown in Eq. (43):

Table 5 Motion characteristics of the mechanism in different phases

Phase	Gaits	
	1.5 m/s, 0 kg	3.0 m/s, 20 kg
Heel strike	20.7°	32.6°
Foot flat	19.8°	30.0°
Heel off	− 2.7°	11.2°
Toe off	− 20.7°	− 3.9°
Swing	− 1.7°~22.1°	11.9°~31.4°

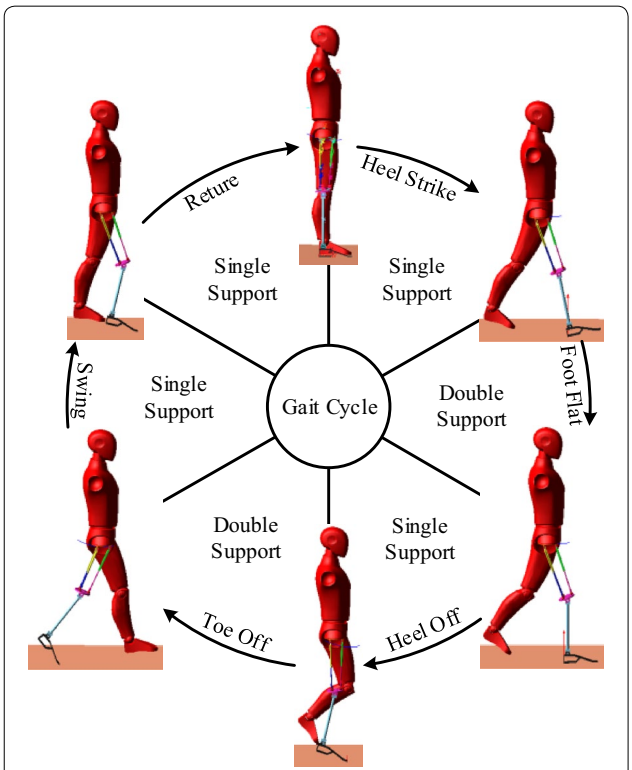

Figure 16 The movements of the prosthetic mechanism in a gait cycle

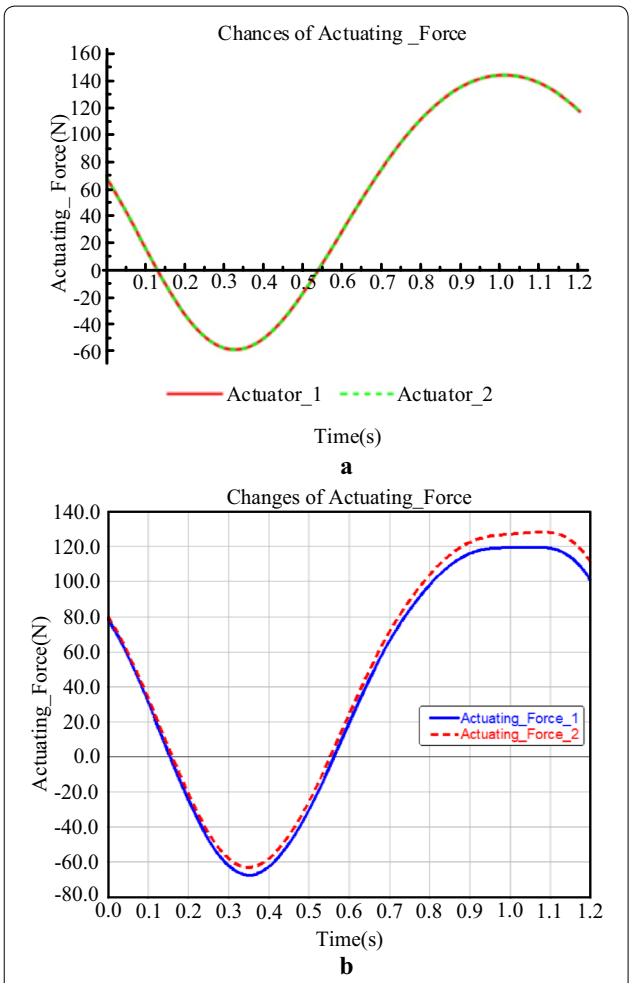

Figure 17 Actuating forces in the first gait mode: **a** actuating forces by Mathematica; **b** actuating forces by Adams

$$\begin{cases} \alpha = \begin{cases} \frac{11\pi}{360}\cos\left(\frac{5\pi}{3}t-\pi\right), & 0 \le t < 0.8, \\ \frac{35\pi}{18}t^2+\frac{31\pi}{9}t+\frac{533\pi}{360}, & 0.8 \le t < 1.0, \\ -\frac{\pi}{36}t+\frac{\pi}{120}, & 1.0 \le t < 1.2, \end{cases} \\ \beta = 0. \end{cases} \tag{43}$$

The *i*th ($i=2,3$) actuating forces versus time calculated by the program are shown in Figure 18a, and the simulation results based on Adams are plotted in Figure 18b.

As can be known from Figure 18, the absolute changes in the theoretical solution and the simulation results were the same in the gait cycle. Due to the symmetrical arrangement of the actuating limbs in the sagittal plane, the direction was opposite.

Furthermore, the theoretical solution was highly similar to the simulation results in the two gait modes. This verified the validity of the dynamic theoretical model of the hip prosthetic parallel mechanism.

7.2 Inverse Kinematic Verification

In order to verify the validity of the inverse kinematics of the hip prosthetic parallel mechanism, which was derived in Section 3. For the first gait mode, the motion trajectory of the moving platform is given in Eq. (42), and the actuating displacement along the limbs could be calculated, as shown in Figure 19.

Results showed that the changes of the actuating displacement were the same during flexion and extension of the hip. There was a displacement error between the theoretical solution and the simulation results in the heel strike phase, which was about 6 mm.

For the second gait mode, the motion trajectory of the moving platform is given in Eq. (43); the actuating displacement along the limbs could thus be solved, as shown in Figure 20.

As can be known from Figure 20, the theoretical solution and the simulation results were the same in the gait cycle. An acceptable error existed between the theoretical

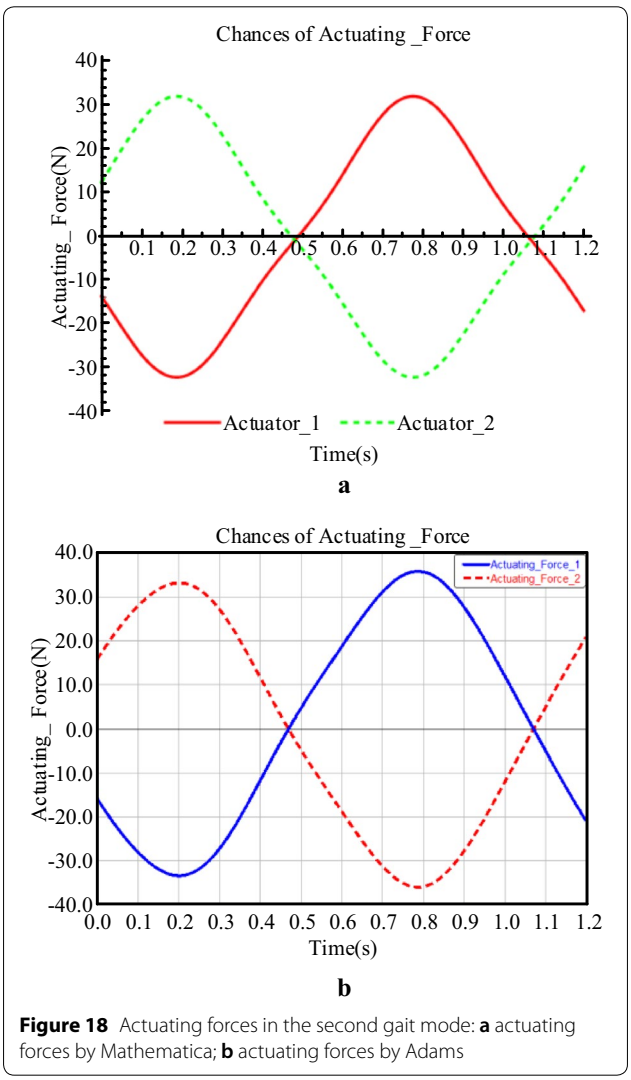

Figure 18 Actuating forces in the second gait mode: **a** actuating forces by Mathematica; **b** actuating forces by Adams

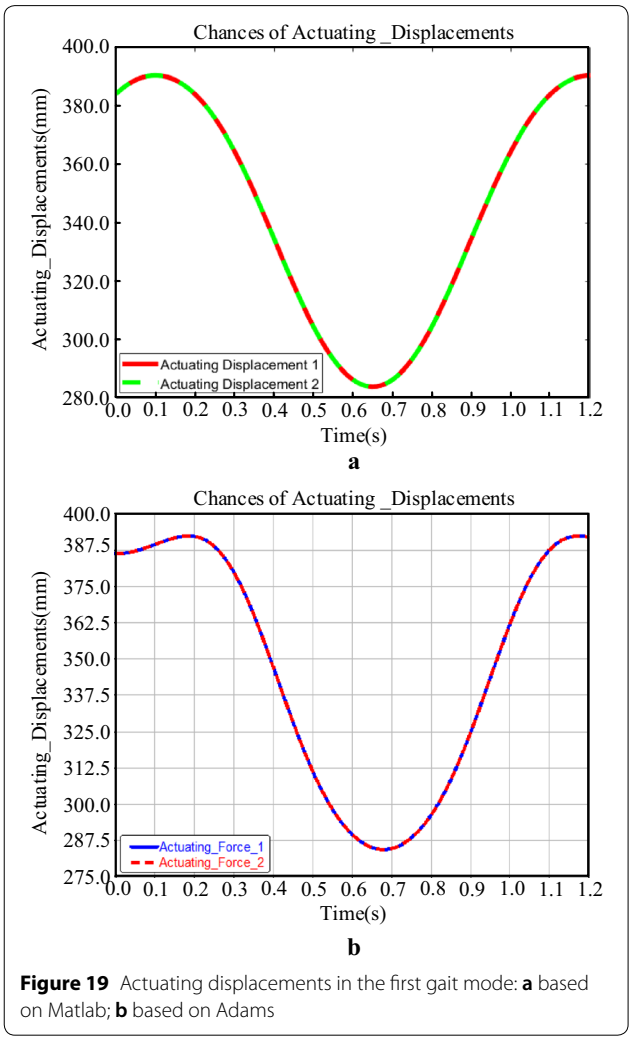

Figure 19 Actuating displacements in the first gait mode: **a** based on Matlab; **b** based on Adams

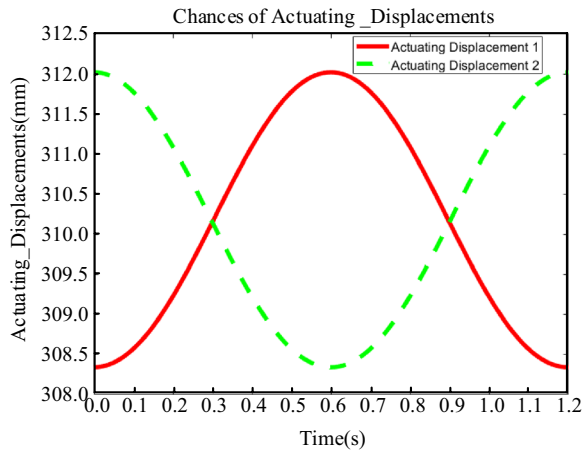

Figure 20 Actuating displacement in the second gait mode: **a** actuating displacement by Matlab; **b** actuating displacement by Adams

solution and the simulation results, which was within 3 mm.

All told, the variation trend in actuating displacements between the theoretical solution and simulation results were highly consistent in the two gait modes, which verified the validity of the inverse kinematics of the hip prosthetic parallel mechanism in Section 3. Moreover, the existence of the error was caused by the deviation between the trajectory equation and the motion curve. Another factor was the inevitable error between the joint of the prosthetic mechanism and the human hip.

7.3 Analysis of the Hip Torque

As can be seen from Figure 15, flexion and extension of the hip are the main motions, which are more important than adduction and abduction.

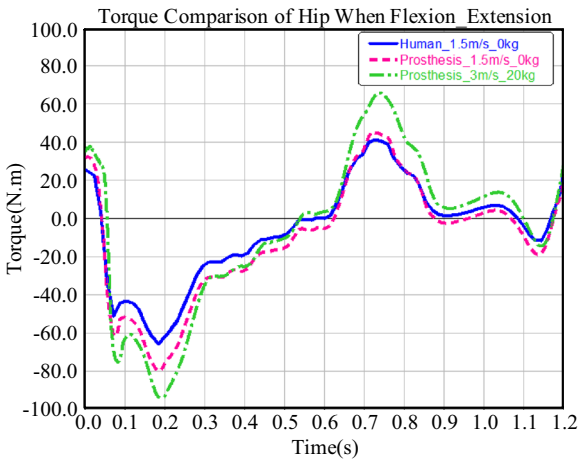

Figure 21 Changes in hip torque in multiple gait modes

Hence, the joint torque during flexion and extension should be considered in the design of the hip prosthetic parallel mechanism.

Based on the human dynamic simulation of an amputee, who wears the 2-UPR/URR hip parallel prosthetic mechanism, the hip torques could be obtained in the multiple gait modes, as shown in Figure 21.

As can be seen from Figure 21, the blue solid line denotes the hip torque of the adult subject at 1.5 m/s walking speed. The magenta dashed line represents the hip torque of the amputee, who wears the prosthetic mechanism, at 1.5 m/s walking speed. The green dot-dash line represents the hip torque of the amputee, who wears the prosthetic mechanism in the first gait mode.

Results showed that the variation tendency of the hip torque was consistent. It verified the feasibility of the 2-UPR/URR parallel mechanism as a hip prosthesis in multiple gait modes. Additionally, the torque changes in the prosthetic mechanism were larger than those in the adult subject in the same gait mode, which may have been caused either by the existence of the geometric error between prosthetic mechanism and the human thigh or the rigid impact between the prosthetic mechanism and the ground.

8 Conclusions

(1) By analysis of the motion characteristics of an adult subject's hip, a novel parallel mechanism with a passive limb, named 2-UPR/URR parallel mechanism, which can realize the movement function of the hip, was designed based on configuration synthesis and screw theory.

(2) The workspace was calculated based on inverse kinematics. The stiffness and dexterity were analyzed in terms of the fully Jacobian matrix. They verified the kinematic feasibility of the 2-UPR/URR parallel mechanism as the hip prosthesis. Furthermore, a statics and buckling analysis were conducted based on the finite element method; the maximum bearing capacity was obtained when the mechanism was stable. The workspace of the proposed prosthetic mechanism was large and its rotational angles covered the requirement of the hip in the four gait modes. Additionally, the prosthesis also had enough stiffness to support the torso, and the maximum bearing capacity was 1376 N, which was greater than the weight of the human body. This indicated that the prosthesis can bear an additional load of 576 N.

(3) The inverse dynamic model of the prosthetic parallel mechanism was constructed by virtual work principle, and Mathematica and Adams were adopted to solve its theoretical solution and simulated results. Moreover, the torques of the prosthetic mechanism, during flexion and extension of the hip, were evaluated based on the human dynamics and compared with the simulation results. Results showed that the actuating forces and actuating displacement were highly similar between the theoretical solution and the simulation results. This verified the validity of the dynamic model and the inverse kinematics of the proposed prosthetic mechanism. Furthermore, the variation trend was consistent between the torques of the prosthetic mechanism and the human hip, which demonstrated the feasibility of the dynamic performance of the 2-UPR/URR parallel mechanism as a hip prosthetic mechanism.

Acknowledgements
All the authors would like to thank the Beijing Natural Science Foundation and National Science Foundation of China for financial support.

Authors' Information
Majun Song, born in 1990, is currently a PhD candidate at *School of Mechanical, Electronic and Control Engineering, Beijing Jiaotong University, China*. He received his master degree from *Jiangxi University of Science and Technology, China*, in 2016. His research interests include parallel robot, medical rehabilitation robot and structural optimization.

Sheng Guo, born in 1972, is currently a professor and a PhD candidate supervisor at *School of Mechanical, Electronic and Control Engineering, Beijing Jiaotong University, China*. His main research interests include spatial mechanism design, parallel robot and medical rehabilitation robot.

Xiangyang Wang, born in 1995, is currently a PhD candidate at *School of Mechanical*, *Electronic and Control Engineering*, *Beijing Jiaotong University*, *China*. His research interests include robotic mechanics, exoskeleton parallel robots.

Haibo Qu, born in 1983, is currently a lecturer at *Robotics Institute, Beijing Jiaotong University, China*. He received his PhD from *Beijing Jiaotong University* in 2013. His research interests include robotics mechanism and mechanical design.

Authors' contributions
SG in charge of the whole trial; MS wrote the manuscript; SG, MS, XW and HQ assisted with sampling and laboratory analyses. All authors read and approved the final manuscript.

Funding
Supported by Beijing Natural Science Foundation (Grant No. L172021), National Natural Science Foundation of China (Grant No. 51875033).

Competing interests
The authors declare no competing financial interests.

Received: 4 July 2019 Revised: 18 December 2019 Accepted: 5 February 2020
Published online: 27 February 2020

References

[1] A H Timemy, G Bugmann, J Escudero, et al. Classification of finger movements for the dexterous hand prosthesis control with surface electromyography. *IEEE Journal of Biomedical and Health Informatics*, 2013, 17(3): 608–618.
[2] Y L Han, S Jia, X S Wang. Design and simulation of an ankle prosthesis with lower power based on human biomechanics. *Robot*, 2013, 35(3): 276–282. (in Chinese)
[3] L M Nelson, T Neil, C P Carbone. Functional outcome measurements of a veteran with a hip disarticulation using a Helix 3D hip joint: A case report. *Journal of Prosthetics and Orthotics*, 2011, 23(1): 21–26.
[4] G Maja, K Roman, A Luka, et al. Online phase detection using wearable sensors for walking with a robotic prosthesis. *Sensors*, 2014, 14: 2776–2794.
[5] R Hanz, S Dan, A S William, et al. Dynamic modeling, parameter estimation and control of a leg prosthesis test robot. *Applied Mathematical Modelling*, 2015, 39: 559–573.
[6] Y N Gu. *Design of humanoid lower limbs mechanism based on a new type of joint and its measurement and control technology research*, Master's Thesis, Yanshan University, Qinhuangdao, China, 2017. (in Chinese)
[7] G Cheng, W Gu, S L Jiang. Singularity analysis of a parallel hip joint simulator based on Grassmann line geometry. *Journal of Mechanical Engineering*, 2012, 48(17): 29–37. (in Chinese)
[8] R Sellaouti, F B Ouezdou. Design and control of a 3-DOFs parallel actuated mechanism for biped hip joint. *Mechanism and Machine Theory*, 2005, 40: 1367–1393.
[9] Q L Wang, J L Liu, S R Ge. Study on biotribological behavior of the combined joint of CoCrMo and UHMWPE/BHA composite in a hip joint simulator. *Journal of Bionic Engineering*, 2009, 6(4): 378–386.
[10] E Joseph, Muscolino, P Li. *Musculoskeletal anatomy coloring book*. Beijing: Beijing Science and Technology Press, 2017. (in Chinese)
[11] J G Qian, Y W Song. *Biomechanics of sports rehabilitation*. Beijing: People's Sports Press, 2015. (in Chinese)
[12] Z Huang, Y S Zhao, T S Zhao. *Advanced spatial mechanism*. Beijing: Higher Education Press, 2006. (in Chinese)
[13] H Saioa, P Charles, A Oscar, et al. Analysis of the 2PRU-1PRS 3-DOF parallel manipulator: Kinematics, singularities and dynamic. *Robotics and Computer-Integrated Manufacturing*, 2018, 51: 63–72.
[14] A J Sameer, L W Tsai. Jacobian analysis of limited-DOF parallel manipulators. *Journal of Mechanical Design*, 2002, 124: 254–258.
[15] B C Hee, R Jeha. Singularity analysis of a four degree-of-freedom parallel manipulator based on an expanded 6×6 Jacobian Matrix. *Mechanism and Machine Theory*, 2012, 57: 52–61.
[16] G J Liu, Z Y Qu, X C Liu, et al. Singularity analysis and detection of 6-UCU parallel manipulator. *Robotics and Computer-Integrated Manufacturing*, 2014, 30: 172–179.
[17] Y Lu, B Hu. Unified Solving Jacobian/Hessian matrices of some parallel manipulators with n-SPS active legs and a passive constrained leg. *Journal of Mechanical Design*, 2007, 129: 1161–1169.
[18] L W Tasi. *Robot analysis: The mechanics of serial and parallel manipulators*. New York: Wiley-Interscience Publication, 1999.
[19] V Kumar. Characterization of workspaces of parallel manipulators. *Journal of Mechanical Design*, 1992, 114: 368–375.

[20] G Coppola, D Zhang, K Liu. A 6-dof reconfigurable hybrid parallel manipulator. *Robotics and Computer-Integrated Manufacturing*, 2014, 30(2): 99–106.
[21] Z Gao, D Zhang. Performance analysis, mapping, and multi-objective optimization of a hybrid robotic machine tool. *IEEE Transactions on Industrial Electronics*, 2015, 62(1): 423–433.
[22] R Lukas, G Nikolai, J B Franz. Sensitivity of structural response in context of linear and nonlinear buckling analysis with solid shell finite elements. *Structural and Multidisciplinary Optimization*, 2017, 55(6): 2259–2283.
[23] J P Merlet. Jocabian, manipulability, condition number and accuracy of parallel robots. *Journal of Mechanical Design*, 2006, 128(1): 199–206.
[24] M J Tasi, H W Lee. Generalized evaluation for the transmission performance of mechanisms. *Mechanism and Machine Theory*, 1994, 29(4): 607–618.
[25] Y P Cheng, Y Cheng. *MATLAB theoretical mechanics*. Beijing: Higher Education Press, 2015. (in Chinese)
[26] Z M Chen, X M Liu, Y Zhang, et al. Dynamics analysis of a symmetrical 2R1T 3-UPU parallel mechanism. *Journal of Mechanical Engineering*, 2017, 53-(21): 46–53. (in Chinese)
[27] H Yang, H R Fang, Y F Fang, et al. Kinematics performance and dynamics analysis of a novel parallel perfusion manipulator with passive link. *Mathematical Problems in Engineering*, 2018, 2: 1–18.
[28] L W Tsai. Solving the inverse dynamics of a Stewart-Gough manipulator by the principle of virtual work. *Journal of Mechanical Design*, 2000, 122: 3–9.
[29] D S Zhang, Y D Xu, J T Yao, et al. Analysis and optimization of a spatial parallel mechanism for a new 5-DOF hybrid serial-parallel manipulator. *Chinese Journal of Mechanical Engineering*, 2018, 31: 54, https://doi.org/10.1186/s10033-018-0251-4.